

High Surface Area Functionalized Nanolaminated Membranes For Energy Efficient Nanofiltration And Desalination In Forward Osmosis

Wensen Wang

Institut Européen des Membranes, IEM, UMR 5635, Université Montpellier, ENSCM, CNRS

Nicolas Onofrio

Institut Européen des Membranes, IEM, UMR 5635, Université Montpellier, ENSCM, CNRS

Eddy Petit

Institut Européen des Membranes, IEM, UMR 5635, Université Montpellier, ENSCM, CNRS

Bonito Karamoko

Institut Européen des Membranes, IEM, UMR 5635, Université Montpellier, ENSCM, CNRS

Huali Wu

Institut Européen des Membranes, IEM, UMR 5635, Université Montpellier, ENSCM, CNRS

Jiefeng Liu

Institut Européen des Membranes, IEM, UMR 5635, Université Montpellier, ENSCM, CNRS

Ji Li

College of Bioresources and Materials Engineering, Shaanxi University of Science & Technology

Kun Qi

Institut Européen des Membranes, IEM, UMR 5635, Université Montpellier, ENSCM, CNRS
<https://orcid.org/0000-0002-5574-4475>

Yang Zhang

Institut Européen des Membranes, IEM, UMR 5635, Université Montpellier, ENSCM, CNRS

Christel Gervais

Sorbonne Université, Collège de France, Laboratoire de Chimie de la Matière Condensée de Paris (LCMCP)

Luc Lajaunie

Departamento de Ciencia de los Materiales e Ingeniería Metalúrgica y Química Inorgánica, Facultad de Ciencias, Universidad de Cádiz, Campus Río San Pedro S/

Chrystelle Salameh

Institut Européen des Membranes, IEM, UMR 5635, Université Montpellier, ENSCM, CNRS

Philippe Miele

Institut Européen des Membranes, IEM, UMR 5635, Université Montpellier, ENSCM, CNRS

<https://orcid.org/0000-0003-3530-8120>

Zhiyuan Zeng

Department of Materials Science and Engineering, City University of Hong Kong

Damien Voiry (✉ damien.voiry@umontpellier.fr)

Institut Européen des Membranes

Article

Keywords:

Posted Date: May 2nd, 2022

DOI: <https://doi.org/10.21203/rs.3.rs-1533962/v1>

License: © ⓘ This work is licensed under a Creative Commons Attribution 4.0 International License.

[Read Full License](#)

1 **High Surface Area Functionalized Nanolaminated Membranes For Energy**
2 **Efficient Nanofiltration And Desalination In Forward Osmosis**

3
4 Wensen Wang¹, Nicolas Onofrio¹, Eddy Petit¹, Bonito Aristide Karamoko¹, Huali
5 Wu¹, Jiefeng Liu¹, Ji Li^{1,2}, Kun Qi¹, Yang Zhang^{1,3}, Christel Gervais,^{4,5} Luc
6 Lajaunie^{6,7}, Chrystelle Salameh¹, Philippe Miele^{1,4}, Zhiyuan Zeng^{8,9}, Damien Voiry^{1*}
7

8 ¹ *Institut Européen des Membranes, IEM, UMR 5635, Université Montpellier,*
9 *ENSCM, CNRS, Montpellier 34000, France*

10 ² *College of Bioresources and Materials Engineering, Shaanxi University of Science &*
11 *Technology, Xi'an 710021, P. R. China*

12 ³ *Key Laboratory of Optoelectronic Devices and Systems of Ministry of Education and*
13 *Guangdong Province, College of Optoelectronic Engineering, Shenzhen University,*
14 *Shenzhen, 518000, China*

15 ⁴ *Institut Universitaire de France (IUF), 1 rue Descartes, 75231 Paris Cedex 05*

16 ⁵ *Sorbonne Université, Collège de France, Laboratoire de Chimie de la Matière*
17 *Condensée de Paris (LCMCP), 4 place Jussieu, 75252 Paris cedex 05, France.*

18 ⁶ *Departamento de Ciencia de los Materiales e Ingeniería Metalúrgica y Química*
19 *Inorgánica, Facultad de Ciencias, Universidad de Cádiz, Campus Río San Pedro S/N,*
20 *Puerto Real, 11510, Cádiz, Spain*

21 ⁷ *Instituto Universitario de Investigación de Microscopía Electrónica y Materiales*
22 *(IMEYMAT), Facultad de Ciencias, Universidad de Cádiz, Campus Río San Pedro*
23 *S/N, Puerto Real 11510, Cádiz, Spain*

24 ⁸ *Department of Materials Science and Engineering, City University of Hong Kong,*
25 *Hong Kong 999077, P. R. China*

26 ⁹ *Shenzhen Research Institute, City University of Hong Kong, Shenzhen 518057, China*
27

28 **Abstract**

29 **Stacking two-dimensional (2D) nanosheets into laminar membranes to create**
30 **nanochannels has attracted widespread attention at fundamental and practical**
31 **levels for separation technology. Constructing space-tunable and long-term stable**
32 **sub-nanometer channels provide original systems for nanofluidic investigations**
33 **and accurate molecular sieving. Although proof-of-concept for nanolaminate**
34 **membranes has recently been demonstrated, uncontrollable swelling and the**
35 **presence of pinholes prevent the scaling up of these membranes. Here, we report**

36 a scalable strategy for the preparation of non-swelling covalently functionalized
37 molybdenum disulfide (MoS₂) membranes with tunable interlayer space. The
38 capillary height of nanochannels was precisely tuned from 3.5 to 7.7 Å, controlled
39 by the nature of the functional groups attached on the MoS₂ nanosheets, which
40 exhibit minimal swelling in water. We evaluated the relationship between the
41 capillary height, the surface chemistry, the stacking disorder and the sieving
42 behaviors of the membranes in forwards osmosis (FO). We found that water
43 permeation is strictly controlled by the capillary height of the nanochannels and
44 the stacking disorder of the nanosheets. By combining experimental investigations
45 and numerical simulations, we identified that the functionalization with aryl
46 groups induces the formation of an interlayer space of 7.1 Å and interlayer
47 stiffness as low as 5.6 eV Å⁻², leading to controlled stacking defects. We report the
48 fabrication of membranes up to 45 cm², which demonstrate a salt rejection as high
49 as 94.2% for a continuous operating time of 7 days. Our work presents a
50 desalination strategy in FO with a specific energy consumption (SEC) of 4 × 10⁻³
51 kWh m⁻³, which compares favorably with commercial FO membranes. We
52 anticipate that this opens avenues for the development of FO membranes for
53 desalination based on nanolaminated structure.

54 55 **Introduction**

56 The construction of selectively permeable membranes with sub-nanometer
57 channels has gained attention for artificial bionics and molecular sieving by taking
58 advantage of the sub-nanometer size of the pores formed between two successive
59 nanosheets. Two-dimensional nanolaminates are regarded from both fundamental and
60 practical points of view as mimicking systems of the biological protein transport

61 channels and building blocks of nanofiltration membranes^{1,2}. In nanolaminated
62 membranes, mass transport typically occurs within the physical gap between the layers
63 defined as the interlayer space or the capillary height. The fabrication of 2D sub-
64 nanometer channels with controlled dimensionality and chemistry of the interlayer
65 space has therefore emerged as a mature topic in the field of 2D materials³⁻⁵. The
66 practical demonstration of nanolaminate membranes has not been achieved due to two
67 main bottlenecks which are (i) the intrinsic instability of the interlayer space and (ii)
68 the difficulty of fabricating pinhole-free membranes on a large scale with controlled
69 thickness.⁶⁻⁸ Currently, the most widely studied 2D building block of nanolaminate
70 membranes is graphene oxide (GO), which forms interlayer spaces of around 5 Å in
71 dry condition. This allows a narrow molecular sieve size with sharp molecular cut-off
72 for rejecting large molecules and ions at the expense of the water flux⁹. Although the
73 space size can be modulated by encapsulating GO membrane into epoxy under different
74 humidity, the process is rather complex and prevents realistic applications¹⁰. Other
75 strategies for controlling the pore size of the nanolaminates include ion coordination¹¹,
76 polymer intercalation¹², crosslinking¹³. Inevitable swelling occurs in pristine GO
77 membrane when it is operated in an aqueous solution, which however dramatically
78 increases the interlayer spacing, leading to a rapid degradation of the sieving
79 performance¹⁴⁻¹⁶. Besides GO, MoS₂ and MXene nanosheets are alternative building
80 block candidates for the construction of 2D nanochannels¹⁷⁻²⁰. MoS₂ laminated
81 membranes have shown outstanding water permeation in reversed osmosis (RO) and
82 the improved stability compared to GO and MXene membranes^{21,22}. Unfortunately, the
83 molecular cutoff of MoS₂ membranes depends on the presence of intercalated water
84 molecules in the laminated structure²³. We have recently reported a facile strategy to
85 modify the surface chemistry of the MoS₂ nanosheets and tune the interlayer space²⁴.

86 Although the vast majority of the efforts have focused on membranes for RO
87 applications, forward osmosis (FO) is regarded as a strategy to reduce the energy
88 footprint associated with water purification processes. To date, only few studies have
89 however focused on producing membranes with sizes greater than 1 cm² due to the
90 difficulty of controlling the integrity of the membrane structures (swelling,
91 delamination, formation of pinholes).

92 Here, using MoS₂ nanosheets as building units, we adopted a chemical
93 functionalization strategy to prepare FO membranes with controlled interlayer space
94 and interlayer stiffness in order to tailor the interlayer space and the stacking disorder
95 in the nanolaminated structure. The membranes are found to be resistant against
96 swelling, while the interlayer space can be adjusted with ångström precision. We
97 demonstrated the fabrication of membranes with thickness from 100 nm up to 1 µm and
98 dimensions as large as 45 cm². The membranes achieved a water flux as high as 12
99 LMH with molecular cutoff of 122 Da and a salt rejection as high as 94.2%. When
100 tested against desalination, the functionalized MoS₂ FO membranes demonstrated
101 superior salt rejection performance for 7 days without significant loss of the water flux
102 compared with GO-based membranes and commercial polymer FO membranes. The
103 nanofluidic behavior of nanofluids in various channels has been studied using physical
104 characterizations and molecular dynamic simulations to unravel the size entanglements
105 of the surface chemistry, the sub-ångström interlayer space and the disorder of the
106 stacking of the nanosheets in the laminated structure. We finally evaluated the energy
107 consumption of our filtration system and found that the MoS₂ nanolaminate membranes
108 may allow for a lower electrical power consumption compared to commercial FO
109 membranes thus opening avenues for practical applications of nanolaminate FO
110 membranes.

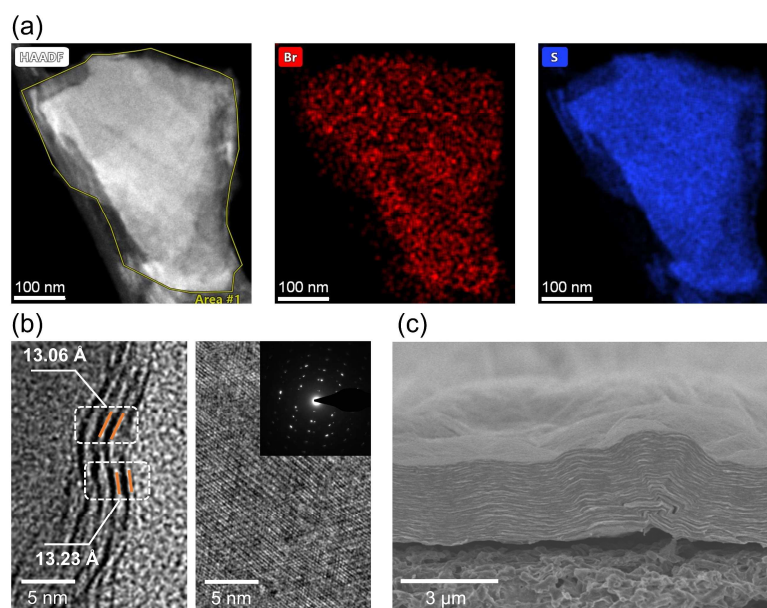
111

112 **Preparation and Characterization of Functionalized MoS₂ Membranes**

113 Molybdenum disulfide nanosheets were exfoliated in water from a bulk crystal
114 using the traditional lithium intercalation method²⁵. To prevent leaching of the
115 functional groups when operating the membranes, covalent functionalization is
116 preferable. The nanosheets were functionalized using alternatively organohalides or
117 diazonium salts in order to covalently attach alkyl and aryl functional groups,
118 respectively. Six types of molecules were selected: iodoethane, 1-iodopropane, ethyl
119 iodoacetate, (2-iodoethyl) benzene, 3-iodo-1-propanol, and 4-bromobenzenediazonium,
120 offering different sizes and polarities, to tune the surface chemistry of the nanosheets.
121 **Figure 1a** shows the images of High-angle annular dark-field imaging Scanning
122 Transmission Electron Microscopy (HAADF-STEM) of 4-bromobenzenediazonium
123 functionalized MoS₂ nanosheets. We performed Energy Dispersive X-ray Spectroscopy
124 (EDX) elemental mapping of bromine to unambiguously confirm the presence of
125 attached functional groups to the nanosheets. The homogeneous contrast suggests a
126 uniform attachment of the aryl groups on MoS₂. High-resolution transmission electron
127 microscopy (HRTEM) images show that the functionalized nanosheets are still
128 crystalline (**Fig. 1b**). The functionalized nanosheets were then characterized by
129 performing Attenuated total reflectance Fourier-transformed infrared (ATR-FTIR),
130 Raman and ¹³C nuclear magnetic resonance (¹³C NMR) spectroscopies. ATR-FTIR and
131 Raman spectroscopies revealed the presence of additional signals or peak splitting after
132 functionalization (See Note and Supplementary Figure 1&2). ¹³C cross-polarization
133 magic angle spinning Nuclear Magnetic Resonance (CP MAS NMR) has been shown
134 to be a powerful tool to probe the nature of the binding on the nanosheets²⁴. ¹³C NMR
135 was carried out on MoS₂ functionalized with ethyl iodoacetate and 4-

136 bromobenzenediazonium salt to confirm the successful covalent attachment of alkyl
137 and aryl groups respectively. **Figures 2a, b** show the chemical shifts of functionalized
138 MoS₂ nanosheets compared with those of the pristine organohalide or diazonium salt
139 reagents. The ¹³C signals of the aliphatic carbon (α -C) at -3.7 ppm²⁶ and 115.3 ppm²⁷
140 for ethyl iodoacetate and 4-bromobenzenediazonium respectively disappear after
141 functionalization and are shifted around 46 ppm and 126 ppm. The significant
142 perturbation of the α -C chemical shifts suggests a new chemical environment, which is
143 attributed to the formation of S-C bonds. The observed chemical shifts of the α -C are
144 also in line with our numerical predictions (Supplementary Figure 3). The degree of
145 grafting of functional groups on the nanosheets was estimated using thermogravimetric
146 analysis (TGA) and the averaged density of functional groups reached ~20 at.% per
147 sulfur (Supplementary Figure 4).

148 The membranes were fabricated by vacuum filtering of the suspension of MoS₂
149 nanosheets on a nylon porous support. Upon the filtration, the nanosheets vertically
150 stack to form a laminated structure. The obtained MoS₂ membranes will be referred to
151 here as C₂-, C₃-, Ace-, Ben-, C₃OH- and Aryl-functionalized MoS₂ membranes
152 corresponding to iodoethane, 1-iodopropane, ethyl iodoacetate, (2-iodoethyl) benzene,
153 3-iodo-1-propanol, and 4-bromobenzenediazonium salt treated MoS₂ nanosheets (**Fig.**
154 **2c**). The ordered interstitial structure was confirmed by the cross-section view of one
155 typical functionalized membrane using scanning electron microscopy (SEM) and X-ray
156 diffraction (XRD) (**Fig. 1c** and **Fig. 2d**). By adjusting the amount of MoS₂ used for the
157 filtration, the membrane thickness was controlled between 100 nm and 1 μ m
158 (Supplementary Figure 5).



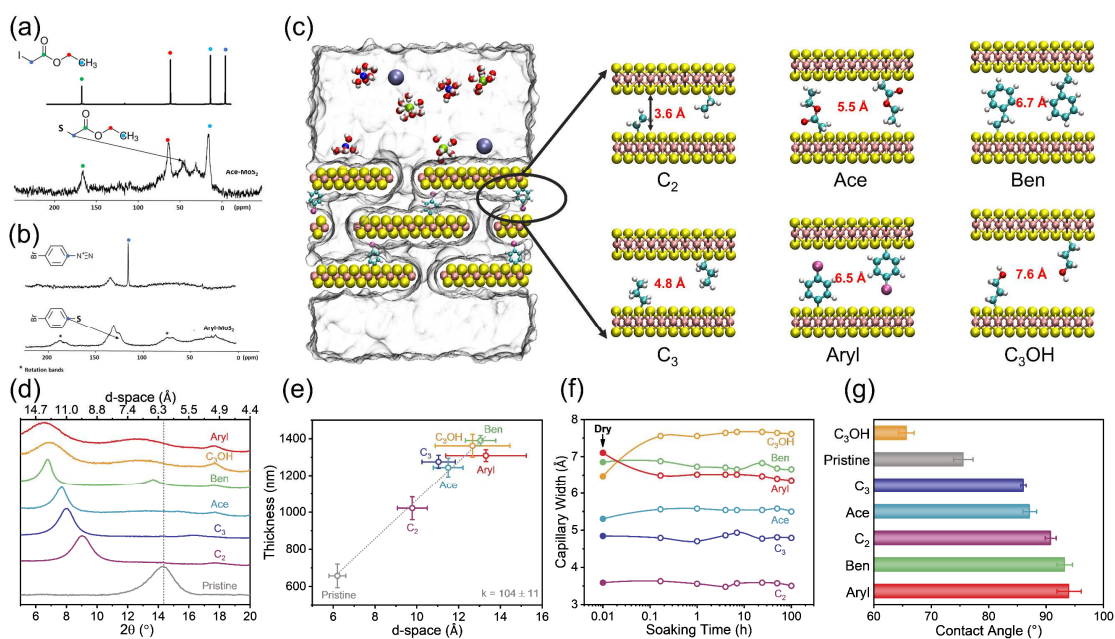
159

160 **Figure 1 | Characterizations of the functionalized MoS₂ nanosheets.** **a**, High-angle
 161 annular dark-field (HAADF) STEM image of 4-bromobenzenediazonium salt
 162 functionalized MoS₂ nanosheets and the corresponding EDX mapping for elements Br
 163 (in red) and S (in blue). The elemental mapping of Br in the functionalized MoS₂
 164 nanosheets shows that the aryl groups are homogeneously grafted on the nanosheets
 165 surface. **b**, HRTEM images of MoS₂ nanosheets functionalized with aryl groups. The
 166 vertically aligned nanosheets form an interlayer spacing of ~13.2 Å, in line with the
 167 XRD measurements. Meanwhile, the crystalline nature of the basal plane of Aryl-MoS₂
 168 nanosheets is confirmed by the diffraction pattern (inset). **c**, The SEM cross-section
 169 view of laminated membrane prepared by vacuum filtration of Aryl-MoS₂ nanosheets
 170 suspension. The highly aligned nanosheets in the vertical direction form 2D capillaries.
 171

172 We then employed XRD to investigate the structure of the nanolaminated MoS₂
 173 membranes (**Fig. 2d**). The XRD pattern from pristine MoS₂ nanolaminates displays an
 174 intense (002) peak at ~14.2° corresponding to a d-space – equivalent to the Mo-to-Mo
 175 distance – of ~6.2 Å. After functionalization, this peak shifts to lower angles
 176 corresponding to an increased interlayer space between the nanosheets. The interlayer
 177 space (capillary height) was estimated by subtracting 6.15 Å corresponding to the Mo-
 178 Mo distance between two layers of MoS₂ in a bulk crystal. We obtained interlayer
 179 spaces of 3.6 Å, 4.8 Å, 5.3 Å, 6.9 Å, 6.5 Å, and 7.1 Å for C₂-, C₃-, Ace-, Ben-, C₃OH-
 180 and Aryl-functionalized MoS₂, respectively. We attribute the increased height of the

181 nanocapillaries to the presence of the grafted functional groups on the surface of the
182 nanosheets acting as nanospacers. Our XRD analyses therefore suggest that the
183 interlayer spacing can be fine-tuned to ångström accuracy by employing different sizes
184 of functional groups. To visually observe the increase of the interlayer space, we
185 measured the evolution of the membrane thickness before and after functionalization
186 (**Fig. 2e** and Supplementary Figure 6). The thickness determined from our SEM cross-
187 section analyses increases linearly with the d-space distance measured from XRD.

188 The structural stability of MoS₂ nanolaminates in aqueous solution was examined
189 by successive *ex-situ* XRD measurement at increased soaking time (Supplementary
190 Figure 7). As shown in **Figure 2f**, the space of hydrophobic nanochannel is found
191 virtually stable in water for over 100 hours. We note that the interlayer space of
192 hydrophilic groups such as (-C₃OH) modified nanochannel experienced a slight
193 increase suggesting some water uptake, which is attributed to the more polar nature of
194 the alkyl chains due to the presence of hydroxyl groups. The swelling is however
195 considerably limited at 8.6% compared to graphene oxide or MXene membranes which
196 showed 94.5% and 22.3% swelling respectively after 100 hours (Supplementary Figure
197 8). Our results indicate that stacking functionalized MoS₂ nanosheets into membranes
198 forms stable nanochannels with finely tunable interlayer space and long-term stability.
199 The changes of surface wettability after MoS₂ functionalization were also examined by
200 water contact angle (WCA) measurements (**Fig. 2g** and Supplementary Figure 9).
201 Compared to pristine membranes, increased WCA values were obtained in the case of
202 hydrophobic groups grafted on the MoS₂, whereas hydrophilic groups caused a
203 decrease in the WCA. The measurements of the WCA brings direct evidence of the role
204 of the surface chemistry to change the physical and chemical behavior of the
205 membranes.



206

207 **Figure 2 | Characterization of the functionalized MoS₂ membranes.** **a** and **b**, ¹³C
 208 CP MAS NMR spectra of the Ace-functionalized (**a**, bottom) and Aryl-functionalized
 209 (**b**, bottom) MoS₂ nanosheets. ¹³C NMR spectra of pure chemical reagents namely ethyl
 210 iodoacetate (**a**, top, solution) and 4-bromobenzenediazonium (**b**, top, solid-state) were
 211 also recorded for comparison. The color dots are used to point out the positions of
 212 carbon atoms in different chemical environments. **c**, Schematic illustration of the
 213 separation process of stacked functionalized MoS₂ membranes with varied capillary
 214 height for water purification and desalination. The values marked in the nanochannels
 215 represent the effective layer space in aqueous solution through which water molecules
 216 can shuttle. Atom color codes: Mo, pink; S, yellow; C, cyan; H, white; O, red; Br,
 217 magenta; Na⁺, blue; Cl⁻, green; Micropollutant, ice-blue; water, transparent gray. **d**, X-
 218 ray diffraction pattern of pristine and functionalized MoS₂ membranes after vacuum
 219 drying for 24 h. **e**, Measured thickness of MoS₂ membranes before and after
 220 functionalization as a function of d-space. The slope *k* multiplied by 10 represents the
 221 number of stacked layers. **f**, Evolution of the capillary height of functionalized MoS₂
 222 membranes in pure water over the soaking time. **g**, The contact angle of pristine and
 223 functionalized MoS₂ membranes. Error bars correspond to standard deviations (s.d.)
 224 based on three independent measurements.

225

226 Ionic Transport and Water Permeation in the Functionalized MoS₂ Membranes

227 We first sought to evaluate the transport of the Na⁺ ions across the functionalized
 228 MoS₂ membranes using a custom-made U-shape cell, where the two-compartments are
 229 filled with an electrolyte solution and DI water, used as permeate and feed solutions,
 230 respectively. We found that compared to water, the transport of Na⁺ is more sensitive

231 to the height of the 2D capillary, and shows an exponential dependence with the
232 capillary height (**Fig. 3a**). The inhibition of Na⁺ transport with decreasing channel size
233 arises from steric hindrance of the pore. The permeation rate for Na⁺ decreased by 20
234 folds as the capillary height decreased from 7.6 Å to 3.6 Å compared to 3 folds for
235 water. In aqueous solution, Na⁺, Cl⁻ and SO₄²⁻ have hydration shells with diameters of
236 7.16 Å, 6.64 Å and 7.58 Å, respectively²⁸. This suggests that to enter inside a narrower
237 channel, the ions will necessarily strip more water molecules, which requires additional
238 energy. It is worth noting that the evolution of the permeation rates of Na⁺ with the
239 capillary height, *i.e.* the slopes in the middle and right panels of **Figure 3a**, is
240 independent from the nature of the counter ions (Cl⁻ or SO₄²⁻). While the faster
241 permeance of Na⁺ (about 3 times) in the case of NaCl compared to Na₂SO₄ is attributed
242 to the larger value of hydration energy for SO₄²⁻: 1330 kJ.mol⁻¹ compared to -420
243 kJ.mol⁻¹ and -350 kJ.mol⁻¹ for Na⁺ and Cl⁻, respectively²⁹. We also found faster
244 permeance rates for Mg²⁺ compared to Na⁺ which is attributed to the Gibbs-Donnan
245 effect due to the presence of remaining excess of charges on the functionalized MoS₂
246 nanolaminates, as confirmed by our zeta potential measurements (Supplementary Table
247 1). Remarkably, our results also indicated a stricter dependence of the permeance with
248 the capillary height, which is attributed to the larger hydrated radius and hydration
249 energy of the Mg ions.

250 The application of hydrostatic pressure in reverse osmosis conditions is known to
251 affect the structure of the capillaries in the nanolaminated structure^{30,31}. Conversely, by
252 operating in FO, we were able to precisely examine the influence of nanochannel
253 structure and surface chemistry on water permeation. We first evaluated the water
254 permeation across the functionalized MoS₂ membranes with different interlayer spaces
255 under forward osmosis (FO) operation. Concentrated KCl (3M) and deionized (DI)

256 water were used as draw and feed solutions, respectively. **Figure 3b** shows the water
257 flux across the functionalized membranes with increasing stacking sequence from 160
258 layers up to 1600 layers in forward osmosis conditions. The pristine – *i.e.* non-
259 functionalized – MoS₂ membranes did not allow water molecules to diffuse due to the
260 narrow capillary height of ~ 0.05 Å (Supplementary Figure 11). Similar water
261 impermeability behavior has been previously reported for MoS₂ membranes tested
262 under reverse osmosis (RO)^{23,32} and highlights to the absence of nanocavities or defects
263 in the laminate structure. In contrast, water permeated through all the functionalized
264 MoS₂ membranes, demonstrating the benefit of functionalization for the diffusion of
265 water. The water flux quickly increased with the decrease of stacking layers due to the
266 shortened pathway for water molecules. We found the highest flux of ~ 12 L h⁻¹ m⁻²
267 (LHM) in the case of Aryl-functionalized membrane with a stacking of 160 layers. This
268 flux is higher than the typical flux for forward osmosis, which is 5~10 LHM^{10,33} .

269 We then sought to discriminate the contribution of the capillary height and the
270 surface chemistry of the nanosheets on the water flux. For a fixed number of MoS₂
271 nanosheets in the nanolaminate, the water flux showed a nearly linear relationship with
272 the capillary height with a ≈ 3 -fold increase when the capillary height increased from
273 3.6 Å to 7.6 Å. This confirms a size-dependent mass transfer process (Supplementary
274 Figure 12). We then extracted the different slopes values for the functionalized
275 membranes when increasing the number of MoS₂ nanosheets from 160 to 1600. The
276 evolution of the water flux in LMH.Å⁻¹ with the number of MoS₂ nanosheets revealed
277 an exponential decrease tendency (**Fig. 3b**, inset). According to the curve fitting, our
278 results predict a flux larger than 100 LMH from a nanolaminate membrane with a
279 capillary height of 7 Å and a stacking sequence of 8 layers of MoS₂, corresponding to
280 a thickness of ≈ 10 nm. This finding highlights the potential of nanolaminate

281 functionalized MoS₂ membranes for FO filtration. A final evidence of the role of the
282 surface chemistry was brought by plotting the water permeance as a function of the
283 WCA. The absence of correlation suggests a rather modest contribution of the surface
284 chemistry and the permeation mechanism is controlled by the structure of the
285 membranes and the interlayer space between the nanosheets in the nanolaminate (see
286 Supplementary Information for details).

287 To better understand the mechanism of water permeation through the size-varied
288 nanochannel, we conducted permeation experiments at different temperatures. As
289 shown in **Fig. 3c**, the permeate flux showed an exponential dependence with
290 temperature in agreement with the Arrhenius law connecting flux and temperature³⁴:

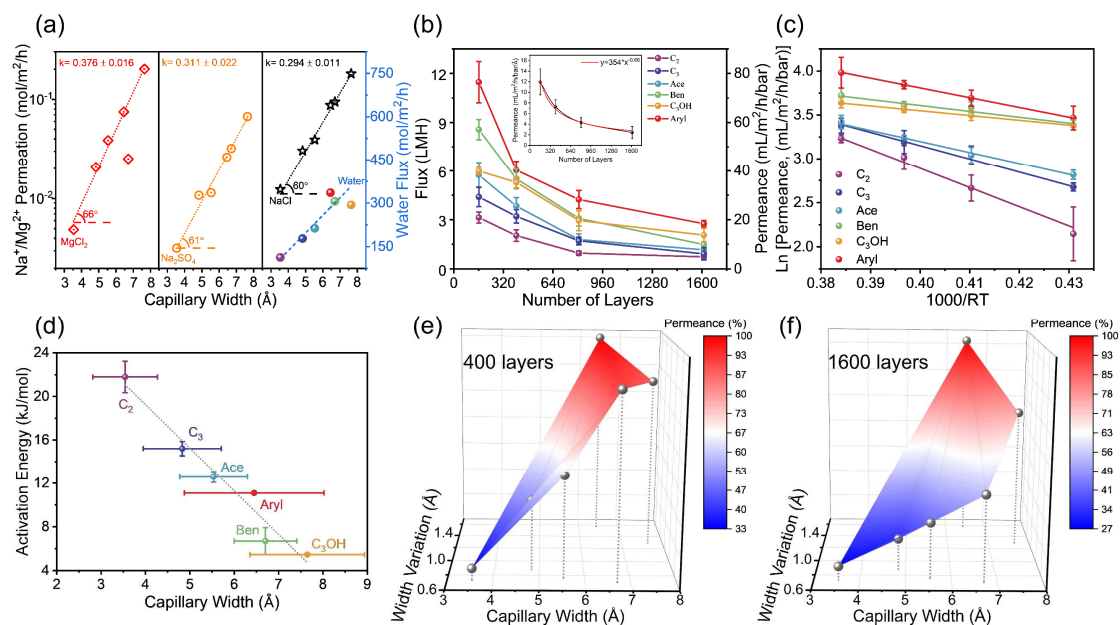
$$291 \quad J = J_0 \exp\left(-\frac{E_a}{RT}\right) \quad (1)$$

292 where J and J₀ represent the water fluxes, R (8.314 J mol⁻¹ K⁻¹) is the gas constant and
293 T (K) is the temperature. E_a represents the activation energy associated with the water
294 permeation, that is, the energy barriers for water to cross the FO membrane. As can be
295 seen from **Figure 3d**, the activation energy of water permeation decreased linearly with
296 capillary height. Hydrophobic ethyl-functionalized membrane with the narrowest
297 channel demonstrated the highest transmembrane energy barriers for water permeation
298 in line with the fact that the membrane exhibits the lowest water flux. With the increase
299 of capillary height, the energy barriers rapidly and continuously decrease, leading to
300 improved water flux. Remarkably, we note that the activation energy of water
301 permeation is less affected by the nature of the functional groups (Supplementary
302 Figure 14). The results clearly point out the role of the sub-nanometer interlayer
303 distance for controlling the energy barriers and the water permeance under FO filtration.
304 It is also worth noting that the Aryl-functionalized membranes showed the highest flux
305 for all thicknesses, while it had moderate energy barriers suggesting that the energy

306 barrier is not the only parameter governing water diffusion in nanolaminates.

307 To elucidate the origin of the apparent high-water flux in Aryl-functionalized MoS₂
308 membranes, we examined the structure of the nanolaminates by comparing the full-
309 height at half-maximum (FWHM) of (002) XRD peaks. The FWHM of the diffraction
310 peaks is known to be a good indicator of the degree of disorder of a crystal and has been
311 used by extension to qualitatively assess the disorder in 2D nanolaminates^{24,35}. The FO
312 membranes made of Aryl-functionalized MoS₂ exhibit the largest FWHM at $1.74^\circ \pm$
313 0.03° , indicating a large variation of capillary height of 1.57 Å (Supplementary Figure
314 15). For comparison, the variation of the capillary height of the corresponding pristine
315 MoS₂ membranes is of only 0.40 Å. The XRD analyses thus suggest a less ordered
316 stacking compared to the other functionalized membranes. A less ordered structure is
317 therefore likely to bring minor tortuosity, leading to a reduced effective path length for
318 water transport, thereby facilitating the water permeation³⁵. To further gauge the
319 influence of the stacking disorder on the water diffusion in the nanolaminate, we plotted
320 the water permeance as a function of capillary height and height variation for
321 nanolaminates with 400 and 1600 nanosheets (**Figs. 3e, f**). We observed that for the
322 thinnest membranes corresponding to a stacking number of 400, the water permeance
323 is controlled by the capillary height, while for thicker laminates the permeance is
324 mainly controlled by the variation in the capillary height. The reduction of the diffusion
325 pathway caused by the decrease of membrane tortuosity is negligible for the thinnest
326 laminates. As the transport pathway increases for thicker membranes, the effect of the
327 tortuosity on the diffusion becomes significant. In light of these results, we identify
328 different behaviors of the nanolaminate FO membranes as the number of two
329 dimensional capillaries increases, which is characterized by a transition from a size-
330 controlled diffusion for the thinnest membranes to disorder-controlled diffusion of the

331 water molecules. Our investigations suggest that the control of both the interlayer space
 332 and the stacking disorder in Aryl-functionalized MoS₂ nanolaminates is responsible for
 333 the superior water flux in FO, making this membrane a relevant candidate for the
 334 realization of practical FO filtration.



335

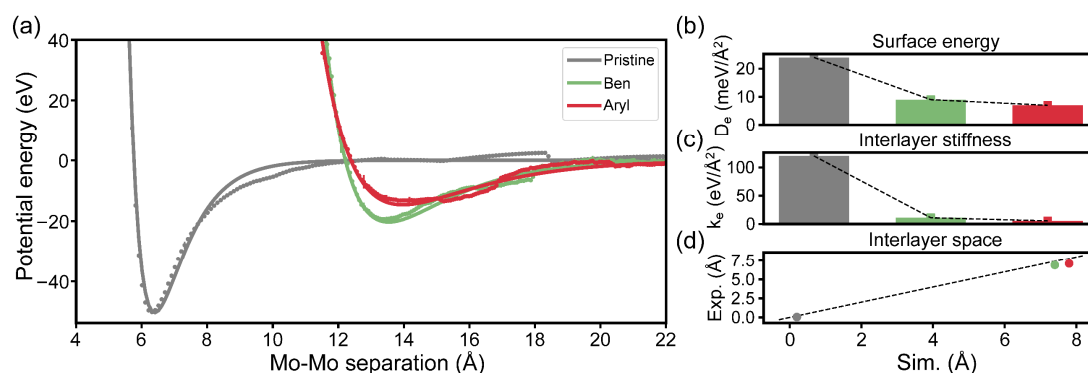
336 **Figure 3 | Water permeation and ionic transport.** **a**, The Na⁺/Mg²⁺ permeation rates
 337 and water flux measured by using 400-layer stacked membranes at room temperature.
 338 1 M NaCl/MgCl₂ or 0.5 M Na₂SO₄ were employed to provide the high ionic strengths
 339 (1 M Na⁺/Mg²⁺) for diffusion. The Na⁺/Mg²⁺ permeation rate depends exponentially on
 340 the capillary height while the water flux varies linearly. Error bars are omitted for clarity.
 341 The dotted lines are best fits. **b**, Water flux of functionalized MoS₂ membranes with
 342 different stacking layers measured at room temperature under forward osmosis, where
 343 3M KCl and DI water were used as the draw and feed solution, respectively. Inset: the
 344 water permeance as a function of membrane thickness. The red curve is the best fit. **c**,
 345 Temperature dependence of water permeation of 400-layer stacked membranes. Solid
 346 lines are best fits to Arrhenius activation energies. **d**, Activation energy of water
 347 permeation for the functionalized MoS₂ membranes as a function of capillary height.
 348 The activation energy varied linearly with capillary height. The dotted line is the best
 349 fit. Vertical error bars correspond to the standard deviation of the measurements. The
 350 horizontal error bars represent the average half-height of the XRD peaks measured after
 351 immersing the membranes in water for a long time (Supplementary Figure 7). **e-f**, The
 352 plotted water permeance of membranes with different stacking numbers (400 layers in
 353 **e** and 1600 layers in **f**) as a function of capillary height and height variation
 354 (Supplementary Figure 15). The permeation rates were normalized by the permeance
 355 of Aryl-functionalized MoS₂ membranes. All the vertical error bars are based on at least
 356 five independent measurements.

357

358 **Mechanical properties of the 2D membranes from MD simulations**

359 The stacking order of the nanolaminate membranes is directly related to the mechanical
360 properties of the layers. Therefore, to get further insight on the atomic origin of the
361 superior water flux of Aryl-functionalized membranes observed above, we performed
362 classical MD simulations of the interaction between functionalized layers (details in the
363 Methods section). Mechanical properties including surface energy and interlayer
364 stiffness can be evaluated by fitting the potential energy of two functionalized layers as
365 a function of interlayer distance, as depicted in **Figure 4a**. Here we use a simple 3-
366 parameters Morse function to fit the potential energy. Our calculations predict surface
367 energies (D_e) of 24, 9 and 6 meV/ \AA^2 , and interlayer stiffnesses (k_e) of 113.7, 11.1 and
368 5.6 eV/ \AA^2 for pristine, Ben- and Aryl-functionalized MoS₂, respectively (see **Fig. 4b**
369 and **c**). We obtained interlayer spaces ($=d_0-6.15$, **Fig. 4d**) of 0.3, 7.4 and 7.8 \AA for
370 pristine, Ben- and Aryl-functionalized MoS₂, respectively, in good agreements with
371 those measured from experiment (0.05, 6.9 and 7.1 \AA , **Fig. 2d**). As expected,
372 functionalization leads to larger interlayer spacing, smaller surface energy as well as
373 smaller interlayer stiffness. Interestingly, we found that for Aryl- functionalized MoS₂,
374 both the surface energy and the interlayer stiffness are about 50 % smaller than for Ben-
375 MoS₂. The small surface energy and the softness of Aryl-MoS₂ layers can be
376 appreciated by the small depth and the flat bottom of the potential well, respectively
377 (**Fig. 4a**). The combination of small surface energy and interlayer stiffness leads to an
378 increase of stacking defects, which contributes to the broadening of the diffraction
379 peaks measured experimentally. Our molecular analysis suggests a direct connection
380 between surface chemistry of the nanosheets and the macroscopic nanofluidic
381 properties of the membranes and it provides a framework for future screening of

382 efficient functional groups for water filtration and desalination.



383

384

385

386

387

388

389

390

391

392

393

394

395

396

397

398

399

400

401

402

403

404

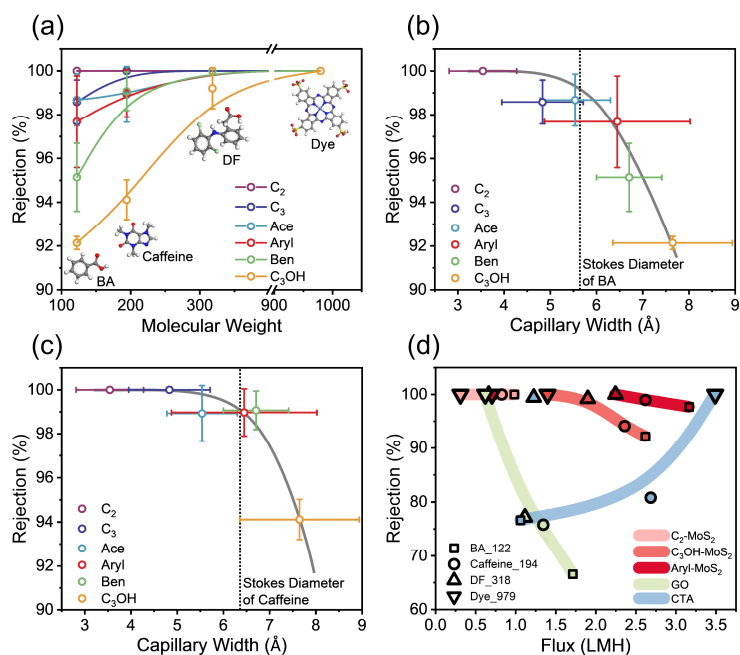
405

Figure 4 | **a**, Potential energy as a function of interlayer separation. To obtain reliable data and statistics, the potential energy surface was scanned 4 times back and forth, as described in the Methods section. Dots correspond to averaged data points and some error bars are displayed (one error bar every 10 averaged data points). Lines correspond to Morse fits as defined by the equation $U(d) = D_e(1 - \exp(-\alpha(d - d_0)))^2$. **b**, Surface energy (D_e). **c**, Interlayer stiffness ($k_e = 2D_e\alpha^2$). **d**, Experimental interlayer space as a function of those ($d_0 - 6.15$) extracted from the Morse fit.

Water Purification and Desalination by Forward Osmosis

To demonstrate the potential of the functionalized MoS₂ membranes, the molecular sieving performance for micropollutants and salt were further evaluated. Four typical micropollutants, a preservative (benzoic acid, BA), a psychoactive drug (caffeine), a common drug (diclofenac sodium, DF) and an organic dye (phthalocyanine), with varied Stoke diameter from ~5.64 Å up to ~14 Å (Supplementary Table 2), were selected and the rejection was measured using high performance liquid chromatography. Rejections of over 90% for all the micropollutants in functionalized membranes were measured, suggesting excellent separation performance in FO. Particularly, the C₂-functionalized membrane with the narrowest channel presented the perfect repulsion of $\approx 100\%$ for the four selected micropollutants. **Figure 5a** shows that the membrane rejection improves with the increase of the molecular weight of the micropollutants in line with the size-limited diffusion as the primary sieving mechanism. When comparing the evolution of the rejection of the micropollutant with the capillary height, we observe

406 a sharp molecular cut-off of the FO MoS₂ membranes (**Fig. 5b, c**). This behavior
407 highlights the importance of controlling the interlayer space and further evidences the
408 absence of pinholes. To benchmark the performance of the functionalized MoS₂
409 membranes, we also estimated the separation performance of the graphene oxide (GO)
410 nanolaminates and a commercial polymeric FO membrane (Cellulose Triacetate, CTA)
411 under the same conditions. As shown in **Figure 5d**, the CTA membrane exhibited both
412 a reduced flux and rejection for the smaller contaminants. We determined a rejection of
413 less than 80% for benzoic acid (BA) in agreement with previous reports from the
414 literature³⁶. Both the rejection and the water permeance rapidly increase when filtering
415 large molecules. This behavior is surprisingly the opposite to those of both GO and
416 MoS₂ FO membranes, which showed a decreased rejection and an increased flux for
417 the smaller micropollutants. The decreased performance for sieving out the smallest
418 molecules hints for a rapid fouling due to the blocking of the one-dimensional
419 nanopores of the polymer membranes. Conversely, nanolaminates exhibit a fouling for
420 the largest molecules due to the deposition of the rejected molecules on the surface of
421 the membranes, while the 2D capillaries are not obstructed (Supplementary Figure 16).
422 The surface fouling of the nanolaminate can however be mitigated by operating under
423 tangential crossflow filtration (as described later in the article). GO membranes also
424 exhibited a poor rejection of 65% for the smallest molecules of BA which is attributed
425 to the large capillary height due to swelling. Overall, owing to the tailored and stable
426 interlayer space, the Aryl-functionalized MoS₂ membranes exhibited superior
427 performance both in rejection and flux than GO and commercial polymer membranes.



428

429 **Figure 5 | Water purification performance of the functionalized MoS₂ membranes.**

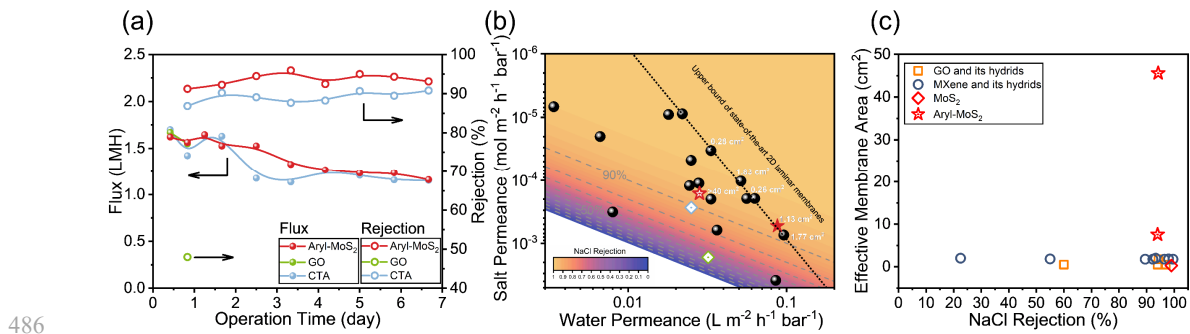
430 **a**, Trace organic contaminants rejection measured with 400-layer stacked
 431 functionalized MoS₂ membranes at 30°C under forward osmosis, where the 2 M sucrose
 432 and 50 mM contaminants (3.3 mM for dye) were used as draw and feed solution. The
 433 rejection is plotted as a function of the molecular weight of contaminants. The insets
 434 show the molecular structure of contaminants and the gray, white, red, blue, green and
 435 yellow balls denote C, H, O, N, Cl and S, respectively. **b** and **c**, Evolution of the
 436 rejection for the benzoic acid (**b**) and caffeine (**c**) with the capillary height of
 437 membranes. The dotted lines represent the effective hydrodynamic diameter of
 438 contaminant molecules (Stokes diameter). The rejection sharply decreases after the
 439 capillary height of membranes are larger than the effective diameter of the
 440 micropollutants, showing size-selective sieving. The solid gray lines are guides to the
 441 eyes. **d**, Comparison of the water purification performance from the functionalized
 442 MoS₂ membranes with GO and commercial FO membrane (CTA). Each symbol
 443 represents the average flux and rejection calculated from at least five independent
 444 measurements and the error bars are omitted for clarity. The complete test data of all
 445 functionalized MoS₂ membranes are shown in Supplementary Figure 16.

446

447 We then examined the performance of the Aryl-functionalized MoS₂ membranes
 448 towards desalination under realistic conditions. FO nanolaminated membranes were
 449 prepared by vacuum filtration with sizes up to 45 cm² and a stacking of 400 layers,
 450 corresponding to a thickness of ≈ 550 nm. We studied the pure water permeance of the
 451 planar 45 cm² Aryl-functionalized membranes by employing a 2M sucrose as draw

452 solution. A stable water flux of 1.3 LMH was achieved under constant flow conditions
453 at room temperature for a period of 7 days (Supplementary Figure 17). The desalination
454 performance of the functionalized MoS₂ membranes was further evaluated on a pilot-
455 scale tangential flow filtration cell under the forward osmosis operation using 0.1 M
456 NaCl as the feed solution (**Fig. 6a**). A water flux greater than 1.6 LMH was achieved
457 and was largely stable over a 7-day period, whereas salt rejection was maintained at
458 greater than $\approx 94.2\%$ and peaked at 96%. These robust desalination properties are
459 attributed to the control of the interlayer distance from the grafted functional groups
460 and the low interlayer stiffness (Supplementary Figure 18). We note that the
461 performance is slightly lower than those obtained using smaller membranes, which
462 demonstrated a water flux of 4.37 LMH with a NaCl rejection of 93.9% suggesting that
463 further improvements can be achieved. We also evaluated the performance of GO
464 membranes and obtained a poor salt rejection of less than 50 % due to the large capillary
465 height of 12.8 Å in line with the literature (Supplementary Figure 8)¹⁰. Importantly, the
466 GO membrane could only run for one day and then rapidly delaminated upon the
467 application of the tangential flow which highlights their intrinsic instability in water³⁷.
468 Besides, commercial CTA polymer membranes exhibited a rejection of around 89.1%
469 with an average flux of 1.25 LMH when tested under the same conditions– consistent
470 with previous reports^{38,39}. Compared with other 2D laminar membranes, the
471 functionalized MoS₂ membranes exhibit a higher water flux and superior salt rejection,
472 exceeding the latest upper bound of state-of-the-art 2D laminar membranes (**Fig. 6b**).
473 Importantly the desalination performance is not significantly affected by the upscaling
474 process and the Aryl-functionalized MoS₂ membranes clearly outperform the best
475 desalination performance from the literature under forward osmosis operation (**Fig. 6c**).
476 We finally evaluated the specific energy consumption (SEC) of our FO system (see

477 Supplementary Information). Under a flow rate of 3.75 mL min^{-1} (1.65 cm s^{-1}), the FO
 478 system recovered 148 mL of water in 20 h, corresponding to a SEC of 0.004 kWh m^{-3} .
 479 This value is lower than previous reports for flat-sheet CTA membranes, which exhibit
 480 SECs of 0.008 kWh m^{-3} and 0.02 kWh m^{-3} , respectively^{40,41}. Although additional
 481 processing of the draw solution is requested to obtain potable water, the present FO
 482 system shows a clear reduction of the energy footprint compared to the other water
 483 recovery approaches such as traditional RO filtration ($1.5\text{-}2.5 \text{ kWh m}^{-3}$)^{42,43}, thermal
 484 distillation technology ($16.3\text{-}27.3 \text{ kWh m}^{-3}$)⁴², and self-supplied FO with thermolytic
 485 ammonium bicarbonate (0.1 kWh m^{-3})⁴⁴.



487 **Figure 6 | Water desalination performance of the functionalized MoS₂ membranes.**
 488 **a**, The desalination performance of Aryl-functionalized MoS₂ membrane and the
 489 comparison with GO and commercial FO membrane. The measurements were
 490 conducted in a tangential cross-flow cell using 2 M sucrose and 0.1 M NaCl as draw
 491 and feed solution. The GO membrane could only be run for one day and then
 492 decomposed. **b**, Comparison of the desalination performance of Aryl-functionalized
 493 MoS₂ (red stars) with other 2D laminar membranes made of GO, MXene and their
 494 hybrids. All the data listed in the figure were measured under separation models in
 495 forward osmosis cells using sucrose and 0.1 M NaCl as draw and feed solution. Our
 496 Aryl-functionalized MoS₂ membranes test data are marked with red stars, while CTA
 497 and GO data are denoted by light-blue and green hollow diamonds. The effective
 498 membrane area is labeled in white. The black line represents the upper bound of state-
 499 of-the-art 2D laminar membranes due to the trade-off between membrane permeability
 500 and selectivity. A comprehensive comparison of desalination performance of 2D
 501 membranes estimated under diffusion or separation models can be found in
 502 Supplementary Table 3. **c**, Comparison of effective membrane area measured in our
 503 work with previously reported membranes.

505 Overall this work presents a robust and scalable method to prepare stable

506 nanolaminated membranes with tunable sieving performance and high water
507 permeance in FO filtration. The structure of the functionalized MoS₂ membranes can
508 be precisely adjusted over a large range of interlayer spaces using alkyl and aryl groups
509 which offers ångström-precision for the 2D nanochannels. Using this approach, we
510 elucidated the contributions from the surface chemistry, the interlayer space and the
511 stacking tortuosity on the behavior of FO nanolaminate membranes. Due to the constant
512 interlayer space in aqueous solution, our functionalized membranes exhibit excellent
513 water purification performance compared with the GO and commercial membranes. In
514 particular, we identified Aryl-functionalized MoS₂ membranes as promising candidates
515 for FO application and demonstrated its scalability up to 45 cm². We believe this is a
516 promising strategy for the design of novel energy-efficient nanofiltration and
517 desalination FO membranes.

518

519 **Methods**

520 *Synthesis of single-layer MoS₂ nanosheets.* The single-layer MoS₂ nanosheets were
521 obtained by exfoliating the bulk MoS₂ powder using the lithium intercalation method.
522 Typically, 400 mg MoS₂ powder and 4 mL n-butyllithium were mixed up in hexane
523 solution and the mixture was stirred at 65°C for 48 h under argon protection. After that,
524 the intercalated powders were collected by vacuum filtration and washed with excessive
525 hexane to remove the unreacted reagent. Then the Li-intercalated powder was added to
526 the water for exfoliation and the process was accelerated by the sonication. After one-
527 hour sonication, the solution was further centrifuged two times at 10,000 g to strip the
528 lithium cations from the nanosheets. In the end, the supernatant containing the single-
529 layer MoS₂ nanosheets was collected after centrifugation twice at 3,000 rpm for 30 min.

530 *Functionalization of single-layer MoS₂ nanosheets.* The single-layer MoS₂

531 nanosheets were modified in solution by reacting with organohalide reagents and
532 diazonium. First, dimethyl sulfoxide (DMSO) was added to the MoS₂ solution to
533 achieve a volume ratio of 3:2. Then the organohalide reagents or diazonium were
534 directly added to the mixture to react for 48h. The excessive organohalide reagents with
535 ten times fold in molar ratio than MoS₂ was added. While the charged diazonium with
536 the same molar amount as MoS₂ was separately added several times to avoid the
537 electrostatic quench and aggregation. Finally, the functionalized MoS₂ solutions were
538 obtained.

539 ***Preparation of functionalized MoS₂ membranes.*** Vacuum filtration was employed to
540 prepare the laminated membranes using diluted functionalized MoS₂ solution. Briefly,
541 a certain amount of MoS₂ solution was filtered on Nylon filter paper with a pore size
542 of 220 nm. After filtration, the membranes were carefully washed 3 times to remove
543 the unreacted reagents. The prepared membranes were dried at room temperature over
544 24 h.

545 ***Water permeation through nanolaminated MoS₂ membranes.*** The pure water flux of
546 nanolaminated MoS₂ membranes was measured using the forward osmosis devices,
547 which consist of two compartments filled with equal volumes (40 mL) of salt solution
548 (3 M KCl) and pure water. The MoS₂ membranes were placed in the middle to separate
549 those two compartments. The volume of salt solution as a draw solution would increase
550 due to the passed water. Based on the increased volume (ΔV) with permeation time (Δt),
551 the water flux could be calculated following the equation:

$$552 \quad J_w = \frac{\Delta V}{A \Delta t} \quad (2)$$

553 Where the A is the effective membrane area (1.13 cm²).

554 ***Ionic permeation through the nanolaminated MoS₂ membranes.*** The Na⁺/Mg²⁺
555 permeation through the 400-layer stacked membranes was measured using two Teflon-

556 made compartments, which were filled with the same volume of DI water and 1 M
557 NaCl/MgCl₂ or 0.5 M Na₂SO₄ solution, respectively. Magnetic stirring was used all the
558 time to eliminate possible concentration gradients around the membranes. The
559 conductivity of the feed side was recorded as a function of permeation time. According
560 to the measured conductivity, the salt concentration of feed side could be calculated
561 using the following equation:

$$562 \quad C = \frac{\kappa}{\Lambda_m} \quad (3)$$

563 where C denotes the salt concentration, κ presents the measured conductivity and Λ_m
564 is the molar conductivity (NaCl: 126.4 S cm² mol⁻¹, MgCl₂: 258.6 S cm² mol⁻¹, Na₂SO₄:
565 259.8 S cm² mol⁻¹)⁴⁵. The salt permeation rate (J) was calculated by:

$$566 \quad J = \frac{VC}{At} \quad (4)$$

567 where V is the solution volume in the feed side (200 mL), C is the calculated
568 concentration from equation (3), A is the surface area of the membrane and t is the
569 permeation time.

570 ***Water purification and rejection evaluations.*** The water purification performances of
571 the membranes were measured using the same apparatus as for the water permeation
572 measurements. However, the draw side and feed side were filled with 2 M sucrose
573 solution and 50 mM micropollutant solution (except for the dye solution, which was
574 3.3 mM), respectively. The two sides were constantly stirred to avoid the concentration
575 polarization. The draw side solution was collected after 20 h and the concentration of
576 micropollutant in sucrose solution was quantitatively analyzed by High-Performance
577 Liquid Chromatography-Ultraviolet (HPLC-UV). The flux was calculated by equation
578 (2) and the rejection was evaluated by the following equation:

$$579 \quad R (\%) = \frac{C_F - C_P}{C_F} \times 100 \quad (5)$$

580 Where C_F and C_P denote the concentration of the feed and permeate solutions,
581 respectively. Unlike the reverse osmosis experiments, the permeated solution in
582 forward osmosis system was diluted by the draw solution. The real concentration of the
583 permeated solution was calculated using the following equation to eliminate the
584 dilution effects:

$$585 \quad C_p = \frac{C_D \times V_D}{V_P} \quad (6)$$

586 Where C_D and V_D are the measured micropollutant concentration in the draw side and
587 the volume of the draw solution. The V_P presents the volume of permeated solution,
588 which is the increased volume in the draw side.

589 ***Water desalination in tangential cross-flow filtration cell.*** We used the tangential
590 cross-flow filtration cell to estimate the water desalination performance of membranes
591 in long-term operation. The membranes with large surfaces were installed in the middle
592 of the pilot-scale forward filtration unit to separate the flowing draw and feed solution.
593 The draw and feed tank were filled with 2 M sucrose solution and 0.58 wt.% NaCl
594 solution, respectively. A peristaltic pump was utilized to provide a constant flow rate
595 of 3.75 mL min^{-1} . Two balances were used to monitor the mass changes of draw and
596 feed tank and the recorded data was further used to calculate the flux. The solutions in
597 the tank were refreshed every 20 h. At the same time, the sucrose solution was collected
598 and the salt concentration was analyzed by Inductively Coupled Plasma Optical
599 Emission Spectrometry (ICP-OES). According to the increased mass and salt
600 concentration in draw side, the salt rejection could be calculated using equations (5)
601 and (6).

602 ***Molecular dynamics simulations parameter.*** Molecular dynamics simulations have
603 been performed with the LAMMPS package⁴⁶ and the OPLS interatomic potential⁴⁷.
604 To describe Mo-S interactions, we use the potential proposed by Blankschtein⁴⁸. We

605 developed OPLS parameters (harmonic bonds, harmonic angles and dihedrals) for S-C
606 interactions between fixed MoS₂ and various organic functional groups. We used a
607 Monte Carlo procedure (similar to that presented in Ref. 49) to optimize OPLS
608 parameters against a training set of density functional theory calculations, as developed
609 in the Supplementary file. Molecular models consist of 2 layers of T' MoS₂ replicated
610 8 and 14 times in the x and y directions, starting from the rectangular unit cell.
611 Functionalization was achieved by randomly grafting functional groups to S atoms until
612 the fraction of 20% groups/S was reached. In order to obtain good statistics on the data
613 points corresponding to the potential energy surface shown in **Figure 4**, we scanned 4
614 times successively the interlayer distance (back and forth). One potential energy surface
615 corresponds therefore to 8 times (4 times back and forth) 300 interlayer distances. At
616 each interlayer distance, the functional groups were randomized by performing 10 ps
617 of NVT simulation at 600 K followed by an energy minimization. We used high
618 temperature MD to provide efficient randomization of the functional groups at each
619 interlayer distances. Although our force field could be used with a larger timestep, we
620 chose a timestep of 0.5 fs in order to properly integrate the equations of motion in the
621 rough conditions of the simulations.

622

623

624 **References**

- 625 1 Shen, J., Liu, G., Han, Y. & Jin, W. Artificial channels for confined mass transport
626 at the sub-nanometre scale. *Nat. Rev. Mater.* **6**, 294-312 (2021).
- 627 2 Werber, J. R., Osuji, C. O. & Elimelech, M. Materials for next-generation
628 desalination and water purification membranes. *Nat. Rev. Mater.* **1**, 1-15 (2016).
- 629 3 Wang, S. *et al.* Two-dimensional nanochannel membranes for molecular and ionic
630 separations. *Chem. Soc. Rev.* **49**, 1071-1089 (2020).
- 631 4 Kang, Y., Xia, Y., Wang, H. & Zhang, X. 2D laminar membranes for selective
632 water and ion transport. *Adv. Funct. Mater.* **29**, 1902014 (2019).
- 633 5 Cheng, L., Liu, G., Zhao, J. & Jin, W. Two-dimensional-material membranes:
634 Manipulating the transport pathway for molecular separation. *Acc. Mater. Res.* **2**,
635 114-128 (2021).
- 636 6 Safaei, J., Xiong, P. & Wang, G. Progress and prospects of two-dimensional
637 materials for membrane-based water desalination. *Mater. Today Adv.* **8**, 100108
638 (2020).
- 639 7 Liu, P. *et al.* Two-dimensional material membranes for critical separations. *Inorg.*
640 *Chem. Front.* **7**, 2560-2581 (2020).
- 641 8 Cheng, Y., Pu, Y. & Zhao, D. Two-Dimensional Membranes: New Paradigms for
642 High-Performance Separation Membranes. *Chem. Asian J.* **15**, 2241-2270 (2020).
- 643 9 Joshi, R. *et al.* Precise and ultrafast molecular sieving through graphene oxide
644 membranes. *Science* **343**, 752-754 (2014).
- 645 10 Abraham, J. *et al.* Tunable sieving of ions using graphene oxide membranes. *Nat.*
646 *Nanotechnol.* **12**, 546-550 (2017).
- 647 11 Chen, L. *et al.* Ion sieving in graphene oxide membranes via cationic control of
648 interlayer spacing. *Nature* **550**, 380-383 (2017).
- 649 12 Shen, J. *et al.* Subnanometer two-dimensional graphene oxide channels for ultrafast
650 gas sieving. *ACS Nano* **10**, 3398-3409 (2016).
- 651 13 Hung, W.-S. *et al.* Cross-linking with diamine monomers to prepare composite
652 graphene oxide-framework membranes with varying d-spacing. *Chem. Mater.* **26**,
653 2983-2990 (2014).
- 654 14 Zheng, S., Tu, Q., Urban, J. J., Li, S. & Mi, B. Swelling of graphene oxide
655 membranes in aqueous solution: characterization of interlayer spacing and insight
656 into water transport mechanisms. *ACS Nano* **11**, 6440-6450 (2017).

- 657 15 Su, P., Wang, F., Li, Z., Tang, C. Y. & Li, W. Graphene oxide membranes:
658 controlling their transport pathways. *J. Mater. Chem. A* **8**, 15319-15340 (2020).
- 659 16 Han, Z.-y. *et al.* A review of performance improvement strategies for graphene
660 oxide-based and graphene-based membranes in water treatment. *J. Mater. Sci.*, 1-
661 30 (2021).
- 662 17 Sun, L., Huang, H. & Peng, X. Laminar MoS₂ membranes for molecule separation.
663 *Chem. Commun.* **49**, 10718-10720 (2013).
- 664 18 Guo, B.-Y. *et al.* MoS₂ membranes for organic solvent nanofiltration: stability and
665 structural control. *J. Phys. Chem. Lett.* **10**, 4609-4617 (2019).
- 666 19 Ren, C. E. *et al.* Charge-and size-selective ion sieving through Ti₃C₂T_x MXene
667 membranes. *J. Phys. Chem. Lett.* **6**, 4026-4031 (2015).
- 668 20 Ding, L. *et al.* A two-dimensional lamellar membrane: MXene nanosheet stacks.
669 *Angew. Chem. Int. Ed. Engl.* **56**, 1825-1829 (2017).
- 670 21 Wang, J. *et al.* Ion sieving by a two-dimensional Ti₃C₂T_x alginate lamellar
671 membrane with stable interlayer spacing. *Nat. Commun.* **11**, 1-10 (2020).
- 672 22 Kim, S., Wang, H. & Lee, Y. M. 2D nanosheets and their composite membranes
673 for water, gas, and ion separation. *Angew. Chem. Int. Ed. Engl.* **131**, 17674-17689
674 (2019).
- 675 23 Wang, Z. *et al.* Understanding the aqueous stability and filtration capability of
676 MoS₂ membranes. *Nano Lett.* **17**, 7289-7298 (2017).
- 677 24 Ries, L. *et al.* Enhanced sieving from exfoliated MoS₂ membranes via covalent
678 functionalization. *Nat. Mater.* **18**, 1112-1117 (2019).
- 679 25 Eda, G. *et al.* Photoluminescence from chemically exfoliated MoS₂. *Nano Lett.* **11**,
680 5111-5116 (2011).
- 681 26 Creemers, A. F. & Lugtenburg, J. The preparation of all-trans uniformly ¹³C-
682 labeled retinal via a modular total organic synthetic strategy. Emerging central
683 contribution of organic synthesis toward the structure and function study with
684 atomic resolution in protein research. *J. Am. Chem. Soc.* **124**, 6324-6334 (2002).
- 685 27 Duthaler, R. O., Förster, H. & Roberts, J. D. Nitrogen-15 and carbon-13 nuclear
686 magnetic resonance spectra of diazo and diazonium compounds. *J. Am. Chem. Soc.*
687 **100**, 4974-4979 (1978).
- 688 28 Nightingale Jr, E. Phenomenological theory of ion solvation. Effective radii of
689 hydrated ions. *J. Phys. Chem.* **63**, 1381-1387 (1959).

- 690 29 Teychené, J., Roux-de Balmann, H., Maron, L. & Galier, S. Investigation of ions
691 hydration using molecular modeling. *J. Mol. Liq.* **294**, 111394 (2019).
- 692 30 Wei, Y. *et al.* Declining flux and narrowing nanochannels under wrinkles of
693 compacted graphene oxide nanofiltration membranes. *Carbon* **108**, 568-575 (2016).
- 694 31 Morelos-Gomez, A. *et al.* Effective NaCl and dye rejection of hybrid graphene
695 oxide/graphene layered membranes. *Nat. Nanotechnol.* **12**, 1083-1088 (2017).
- 696 32 Hoenig, E. *et al.* Controlling the Structure of MoS₂ Membranes via Covalent
697 Functionalization with Molecular Spacers. *Nano Lett.* **20**, 7844-7851 (2020).
- 698 33 Chekli, L. *et al.* A comprehensive review of hybrid forward osmosis systems:
699 Performance, applications and future prospects. *J. Memb. Sci.* **497**, 430-449 (2016).
- 700 34 Wang, K. Y., Chung, T.-S. & Qin, J.-J. Polybenzimidazole (PBI) nanofiltration
701 hollow fiber membranes applied in forward osmosis process. *J. Memb. Sci.* **300**, 6-
702 12 (2007).
- 703 35 Lu, X. *et al.* Relating selectivity and separation performance of lamellar two-
704 dimensional molybdenum disulfide (MoS₂) membranes to nanosheet stacking
705 behavior. *Environ. Sci. Technol.* **54**, 9640-9651 (2020).
- 706 36 Alturki, A. *et al.* Performance of a novel osmotic membrane bioreactor (OMBR)
707 system: flux stability and removal of trace organics. *Bioresour. Technol.* **113**, 201-
708 206 (2012).
- 709 37 Andreeva, D. V. *et al.* Two-dimensional adaptive membranes with programmable
710 water and ionic channels. *Nat. Nanotechnol.* **16**, 174-180 (2021).
- 711 38 Al-aibi, S., Mahood, H. B., Sharif, A. O., Alpay, E. & Simcoe-Read, H. Evaluation
712 of draw solution effectiveness in a forward osmosis process. *Desalination Water*
713 *Treat.* **57**, 13425-13432 (2016).
- 714 39 Li, G., Li, X.-M., He, T., Jiang, B. & Gao, C. Cellulose triacetate forward osmosis
715 membranes: preparation and characterization. *Desalination Water Treat.* **51**, 2656-
716 2665 (2013).
- 717 40 Zou, S. & He, Z. Enhancing wastewater reuse by forward osmosis with self-diluted
718 commercial fertilizers as draw solutes. *Water Res.* **99**, 235-243 (2016).
- 719 41 Lambrechts, R. & Sheldon, M. Performance and energy consumption evaluation of
720 a fertiliser drawn forward osmosis (FDFO) system for water recovery from brackish
721 water. *Desalination* **456**, 64-73 (2019).
- 722 42 Al-Karaghoul, A. & Kazmerski, L. L. Energy consumption and water production

- 723 cost of conventional and renewable-energy-powered desalination processes. *Renew.*
724 *Sustain. Energy Rev.* **24**, 343-356 (2013).
- 725 43 Shannon, M. A. *et al.* Science and technology for water purification in the coming
726 decades. *Nanoscience and technology: a collection of reviews from nature Journals*,
727 337-346 (2010).
- 728 44 Qin, M. & He, Z. Self-supplied ammonium bicarbonate draw solute for achieving
729 wastewater treatment and recovery in a microbial electrolysis cell-forward osmosis-
730 coupled system. *Environ. Sci. Technol. Lett.* **1**, 437-441 (2014).
- 731 45 Horvath, A. L. *Handbook of aqueous electrolyte solutions*. (Halsted Press, 1985).
- 732 46 Plimpton, S. Fast parallel algorithms for short-range molecular dynamics. *J.*
733 *Comput. Phys.* **117**, 1-19 (1995).
- 734 47 Jorgensen, W. L., Maxwell, D. S. & Tirado-Rives, J. Development and testing of
735 the OPLS all-atom force field on conformational energetics and properties of
736 organic liquids. *J. Am. Chem. Soc.* **118**, 11225-11236 (1996).
- 737 48 Sresht, V. *et al.* Quantitative modeling of MoS₂-solvent interfaces: predicting
738 contact angles and exfoliation performance using molecular dynamics. *J. Phys.*
739 *Chem. C* **121**, 9022-9031 (2017).
- 740 49 Onofrio, N. & Ko, T. W. Exploring the Compositional Ternary Diagram of Ge/S/Cu
741 Glasses for Resistance Switching Memories. *J. Phys. Chem. C* **123**, 9486-9495
742 (2019).

743
744

745 **Acknowledgments**

746 This research study was supported by the French National Agency (ANR, program 2D-
747 MEMBA - ANR-21-CE09-0034-01). D.V., K.Q., and H. W. acknowledge funding
748 from the European Research Council (ERC) under the European Union's Horizon 2020
749 research and innovation programme (grant agreement no. 804320). W.W., J.Liu and
750 J.Li acknowledge PhD scholarship from the China Scholarship Council (CSC). C.S.
751 acknowledged funding from the French National Agency (ANR, JCJC program,
752 MONOMEANR-20-CE08-0009). K.Q. and Y.Z. acknowledge financial support from
753 the China Postdoctoral Science Foundation (2018M633127) and the Natural Science

754 Foundation of Guangdong Province (2018A030310602). J.Li acknowledge financial
755 support by the National Natural Science Foundation of China (21808134). The French
756 Région Ile de France - SESAME program is acknowledged for financial support (700
757 MHz NMR spectrometer). This work was granted access to the HPC resources of
758 IDRIS under the allocation 2021-2022-A0110913046 and 097535 made by GENCI.
759 L.L. acknowledges funding from the Andalusian regional government (FEDER-UCA-
760 18-106613), the European Union's Horizon 2020 research and innovation program
761 (grant agreement 823717 – ESTEEM3) and the Spanish Ministerio de Economía y
762 Competitividad (PID2019-107578GA-I00). The (S)TEM measurements were
763 performed at the National Facility ELECMI ICTS ("Division de Microscopia
764 Electronica", Universidad de Cadiz, DME-UCA).

765

766

767 **Author Contributions**

768 D.V. conceived the idea, designed the experiments and wrote the manuscript. W.W.
769 designed the experiments with D.V., synthesized the functionalized nanosheets,
770 fabricated the membranes and performed the experiments. D.V. and W.S. analyzed the
771 data and wrote the manuscript. N.O. performed the atomistic calculations and discussed
772 the results with D.V. and W.W.. B.A.K. assisted W.S. with the measurements and
773 synthesized MXene. E.P. performed the liquid NMR and HPLC-UV to quantify the
774 membrane rejection, while H.W., J.Liu, J.Li, K.Q. and Y.Z. and assisted W.W with the
775 WCA, Raman, FTIR measurements. L.L. performed the (S)TEM measurements and
776 analyzed the data. C.G. performed the solid ¹³C NMR spectroscopy measurements and
777 discussed with results with C.S.. P.M. and Z.Z. discussed the results with W.W. and
778 D.V. All of the authors edited the manuscript before submission.

779

780 **Data availability**

781 The data that support the plots within this paper and other findings of this study are
782 available from the corresponding authors upon reasonable request.

783

784 **Competing financial interests**

785 The authors declare no competing financial interests.

786

787 **Additional Information**

788 **Supplementary information** and chemical compound information are available in the
789 online version of the paper.

790 **Correspondence and requests for materials** should be addressed to D.V.
791 (damien.voiry@umontpellier.fr).

792

Supplementary Files

This is a list of supplementary files associated with this preprint. Click to download.

- [SupportingInformationSubmitNumberLine1.pdf](#)